

Turbulent stresses as a function of shear rate in a local disk model

A. J. Liljeström^{1,*}, M. J. Korpi¹, P. J. Käpylä¹, A. Brandenburg², and W. Lyra³

¹ Observatory, University of Helsinki, PO BOX 14, FI-00014 University of Helsinki, Finland

² NORDITA, AlbaNova University Center, Roslagstullsbacken 23, SE-10691 Stockholm, Sweden

³ Department of Physics and Astronomy, Uppsala Astronomical Observatory, Box 515, 751 20 Uppsala, Sweden

Received 15 Jul 2008, accepted 11 Nov 2008

Key words accretion, accretion disks – instabilities – magnetohydrodynamics (MHD) – turbulence

We present local numerical models of accretion disk turbulence driven by the magnetorotational instability with varying shear rate. The resulting turbulent stresses are compared with predictions of a closure model in which triple correlations are modelled in terms of quadratic correlations. This local model uses five nondimensional parameters to describe the properties of the flow. We attempt to determine these closure parameters for our simulations and find that the model does produce qualitatively correct behaviour. In addition, we present results concerning the shear rate dependency of the magnetic to kinetic energy ratio. We find both the turbulent stress ratio and the total stress to be strongly dependent on the shear rate.

© 2006 WILEY-VCH Verlag GmbH & Co. KGaA, Weinheim

1 Introduction

Since the work of Balbus & Hawley (1991) it is now generally accepted that turbulence in accretion disks is caused by the linear magneto-rotational instability (hereafter MRI) that was originally discovered by Velikhov (1959) in connection with Couette flow of liquid metals. This linear instability can be excited in sufficiently ionized, differentially rotating fluids where the angular momentum decreases with increasing radius. When the fluid is threaded by a magnetic field, differential rotation causes stretching of the field lines. The tension that builds up opposes the shearing, acting to enforce rigid rotation. If the field is subthermal, the interplay between differential rotation and magnetic tension destabilizes the fluid, resulting in linear growth of Reynolds and Maxwell stresses, which transport angular momentum outwards. The instability eventually leads to a fully turbulent, non-linear state.

Let us assume a rotation profile of the form $\Omega \propto r^{-q}$, where Ω is the angular velocity at distance r . A necessary condition for the MRI to be excited is $q > 0$, i.e. the angular velocity decreases outward. The Keplerian case with $q = 1.5$ has been extensively studied by means of numerical simulations making use of the shearing box approximation (e.g., Hawley, Gammie & Balbus 1995, 1996; Brandenburg et al. 1995; Johansen & Klahr 2005), as well as in global disks (e.g. Armitage 1998; Hawley 2001; Lyra et al. 2008). These studies have shown that the MRI leads to a fully turbulent saturated state in which the Maxwell stress is responsible for the majority (about 80%) of the angular momentum transport. Even in the absence of vertical density stratification a turbulent small-scale magnetic field can be main-

tained by dynamo action (Hawley et al. 1996). When stratification is present, cyclic large-scale dynamo action can be excited (Brandenburg et al. 1995).

The dependence of Reynolds and Maxwell stresses on the shear rate has been investigated numerically by Abramowicz, Brandenburg & Lasota (1996) in the presence of stratification and Hawley, Balbus & Winters (1999) in the absence of stratification. It turns out that near $q = 0$ the Reynolds stress, which couples to the large-scale vorticity $W = (2 - q)\Omega$, is small due to the strong stabilizing effect of the vorticity (Hawley et al. 1999). This makes the Maxwell to Reynolds stress ratio very high. As the shear rate $q\Omega$ increases, the shear-coupled Maxwell and Reynolds stresses increase due to the decrease of the vorticity. However, the growth of the Reynolds stress is significantly faster, so the stress ratio diminishes with increasing q .

The interest in MRI-generated turbulent stresses as a function of q was rekindled in a recent study where a linear analysis of the Reynolds and Maxwell stresses was presented (Pessah, Chan & Psaltis 2006a, hereafter PCP06). They derived a simple relation for the stress ratio, depending only on the shear parameter q . Comparing this result with the non-linear simulations of Hawley et al. (1999), they find that, even in the saturated turbulent regime, the stress ratio does indeed depend almost entirely on q alone, and that there is only a weak dependence on other properties of the flow or on the initial conditions.

The Shakura-Sunyaev viscosity parameter α (Shakura & Sunyaev 1973) is still a popular tool to link accretion disk observations to theory. The so-called α model of disks is based on the assumption that the turbulent stresses $T_{r\phi}$ scale linearly with the thermal pressure; $\alpha \leq 1$ being the proportionality factor. In this formalism, the outward trans-

* Corresponding author: e-mail: anne.liljestrom@helsinki.fi

port of angular momentum is characterized by a turbulent viscosity of the form

$$\nu_t = \alpha c_s H, \quad (1)$$

where the eddy viscosity is assumed to scale with the sound speed c_s and the correlation length with the disk scale height H .

As this model linearizes the turbulent system into a standard Navier-Stokes fluid suitable for analytical manipulation, it has been an invaluable tool in developing theory of accretion disk dynamics, even though the parametrization offers no explanation of what is causing the viscosity. Even after the realization of the astrophysical importance and subsequent reinvigorated interest in the theory of the MRI, the α -model is still widely used.

New, more physically motivated models have been developed recently to describe the angular momentum transport in accretion disks (e.g. Kato & Yoshizawa 1995; Pessah, Chan & Psaltis 2006b; Ogilvie 2003, hereafter O03). A common characteristic of these models is the treatment of the problem of angular momentum transport: the governing magnetic and kinetic equations are divided into linear and non-linear terms. The non-linear correlation functions are then modelled by closing the system of equations with approximate expressions that still embody the physics but are considerably easier to solve (such closure models are commonly used in modelling turbulence; see references in O03). It should be noted that the α -model is mathematically equivalent to the simplest closure model, where the correlation functions are modelled by one single coefficient. All these models also operate in the absence of mean magnetic fields. A first attempt to validate the O03 model was made by Garaud & Ogilvie (2005) in connection with shear flow where linear and non-linear instabilities were found to be well reproduced by the model.

In the present study, the turbulent stresses are extracted as functions of q from non-stratified local numerical models with zero net flux using the shearing box approximation. The simulation data are compared with the linear results of PCP06 and the non-linear closure model of O03. There are a few other closure models that describe the behaviour of local, magnetohydrodynamic turbulence. In particular, the model of Pessah et al. (2006b) assumes a uniform vertical field in the disk which is not incorporated in our three-dimensional simulations. Therefore we concentrate here mainly on the closure model of O03.

The remainder of the paper is organised as follows: in Sections 2, 3, and 4 the linear MRI model of Pessah et al. (2006b), the non-linear closure model of O03, and the numerical model are presented, respectively. Furthermore, the results and related discussion are presented in Sections 5 and 6.

2 Stress ratio in the model of PCP06

Here we briefly summarize the formalism employed in the model of PCP06. Using the kinematic hydromagnetic equa-

tions, PCP06 calculated the ratio of the relevant components of Reynolds and Maxwell stresses in a local approximation. We use here a Cartesian frame of reference, where x , y and z denote the radial, toroidal and vertical directions, respectively. The relevant component of the stress tensor is then T_{xy} , which can be decomposed as

$$T_{xy} \equiv R_{xy} - M_{xy}, \quad (2)$$

where

$$R_{ij} = \langle \rho u_i u_j \rangle, \quad M_{ij} = \langle b_i b_j \rangle / \mu_0, \quad (3)$$

are the Reynolds and Maxwell stresses, respectively, and \mathbf{u} is the departure from the mean flow, \mathbf{b} is the departure from the mean magnetic field, ρ is the density, μ_0 the vacuum permeability, and angular brackets denote a suitable volume average. Throughout our paper, compressibility effects are ignored in the turbulence models, i.e. $\rho = \rho_0$ is assumed constant, even though the simulations are fully compressible. The rms velocity in our simulations remains considerably smaller than unity and the flow is therefore subsonic.

Using linear theory, PCP06 found that for given wavenumber k the stress ratio is given by

$$-\frac{M_{xy}(k)}{R_{xy}(k)} = 1 + \frac{2(2-q)\Omega_0^2}{k^2 v_A^2 + \gamma_k^2}, \quad (4)$$

where Ω_0 is the angular velocity, $v_A = B_0 / \sqrt{\mu_0 \rho_0}$ is the Alfvén speed based on a constant vertical magnetic field, and γ_k is the corresponding growth rate of the mode with wavenumber k . Moreover, for the fastest growing mode with

$$\gamma_{k_{\max}} / \Omega_0 = \frac{1}{2}q, \quad v_A^2 k_{\max}^2 / \Omega_0^2 = q - \frac{1}{4}q^2, \quad (5)$$

they find

$$-\frac{M_{xy}}{R_{xy}} = \frac{4-q}{q}. \quad (6)$$

This expression shows that, for the relevant case with $q < 2$, the magnitude of the Maxwell stress is always larger than that of the Reynolds stress. This formula provides a strikingly simple prediction of the stress ratio which is in good agreement with simulation data, even if there is no imposed magnetic field (PCP06). One envisages that the relevant wavenumber is able to adjust itself to the value where the growth rate is maximal.

3 The O03 closure model

The local closure model of O03 includes the linear interaction of the turbulent stress tensors with shear and rotation. The linearized evolution equations for the Maxwell and Reynolds stresses can be derived directly from the basic MHD equations and are fairly straightforward to solve numerically. For modelling the non-linear triple correlations of fluctuating quantities and the small-scale diffusion, five dimensionless, positive definite coefficients appear in the closed system of equations. A closure model is needed to deal with these non-linear terms which are described by

physical effects and constrained by symmetry properties and dimensional considerations.

The five closure coefficients stand for the turbulent dissipation of the Reynolds stresses (C_1), their isotropization (C_2), the effect of the small-scale Lorentz-force as a source for R_{ij} combined with a sink for M_{ij} (C_3), a source due to small-scale dynamo for M_{ij} combined with a sink for R_{ij} (C_4), and turbulent dissipation of the Maxwell stresses (C_5).

The evolution equations of this model are given by

$$\partial_t R_{ij} = -\mathcal{L}_{ij}^R - \tau^{-1} \rho_0^{-1/2} (\mathcal{N}_{ij}^R + \mathcal{I}_{ij}), \quad (7)$$

$$\partial_t M_{ij} = \mathcal{L}_{ij}^M + \tau^{-1} \rho_0^{-1/2} \mathcal{N}_{ij}^M, \quad (8)$$

where $\tau = L/U$ is the turnover time, $U = R^{1/2}$ is the rms velocity, L is the typical scale of the energy-carrying eddies, and

$$R \equiv R_{ii} = \langle \rho(u_x^2 + u_y^2 + u_z^2) \rangle, \quad (9)$$

$$M \equiv M_{ii} = \langle b_x^2 + b_y^2 + b_z^2 \rangle / \mu_0, \quad (10)$$

are the traces of tensors R_{ij} and M_{ij} . Furthermore, \mathcal{L}_{ij}^σ and \mathcal{N}_{ij}^σ are linear and nonlinear terms, respectively, for $\sigma = R$ or M , and are given by

$$\mathcal{L}_{ij}^R = R_{ik} \bar{U}_{j,k} + R_{jk} \bar{U}_{i,k} + 2\Omega_k (\varepsilon_{jkl} R_{il} + \varepsilon_{ikl} R_{jl}), \quad (11)$$

$$\mathcal{L}_{ij}^M = M_{ik} \bar{U}_{j,k} + M_{jk} \bar{U}_{i,k}, \quad (12)$$

$$\mathcal{N}_{ij}^R = (C_1 + C_4 B^2) R_{ij} - C_3 B M_{ij}, \quad (13)$$

$$\mathcal{N}_{ij}^M = C_4 B^2 R_{ij} - (C_3 + C_5) B M_{ij}, \quad (14)$$

where $B = (M/R)^{1/2}$ is the ratio of rms magnetic and velocity fields,

$$\mathcal{I}_{ij} = C_2 (R_{ij} - \frac{1}{3} R \delta_{ij}) \quad (15)$$

is an isotropization term, and $C_1 \dots C_5$ are positive constants that are of the order of unity. Advection operators of the form $\bar{U}_k \partial_k$ have been neglected. The contribution of the advection terms vanish under fully periodic boundary conditions on average so they make no contribution. Note also that τ and B are time-dependent, because R and M are time-dependent.

A similar model for the hydrodynamic case has recently been used to model the generation of shear in rotating anisotropic turbulence by the Λ effect; see Käpylä & Brandenburg (2008) for details. An important difference is that in their model the flow was driven by an external body force, so the equations for the evolution of the Reynolds stress have a corresponding forcing term as well. Such a term is here absent, because the turbulence is solely the result of shear flow instabilities and are modelled by the equations of O03 without external forcing. As explained by O03, the model also predicts turbulence for $q < 0$, where simulations have not shown self-excited turbulence. The reason for this is that O03 do not specifically model the MRI dynamics.

In the present study the large scale velocity is given by the shear flow $\bar{U} = U_0 = -q\Omega_0 x \hat{e}_y$. We abbreviate the parameter combination C_i/L of O03 by c_i . O03 gave an

analytic solution for the hydrodynamic case. Here we give a partial solution for the components of the two stresses if R and M are known. In the steady state, the equations yield for the Reynolds stresses

$$R_{xx} = RA \left(\frac{1}{3} c_2 + Q \right), \quad (16)$$

$$R_{yy} = RA \left(c_1 + \frac{1}{3} c_2 + a B^2 c_5 - Q \right), \quad (17)$$

$$R_{zz} = \frac{1}{3} RA c_2, \quad (18)$$

$$R_{xy} = \frac{R^{1/2}}{2q\Omega} [c_1 R - (B c_3 - c_4) M]. \quad (19)$$

where we have introduced the abbreviations

$$A = (c_1 + c_2 + a B^2 c_5)^{-1}, \quad a = \frac{c_4}{c_3 + c_5}, \quad (20)$$

and

$$Q = \frac{2}{q} [c_1 - B^2 (B c_3 - c_4)]. \quad (21)$$

The components of the Maxwell stress tensor can be expressed in terms of the corresponding components of the Reynolds stress tensor as

$$M_{xx} = a B R_{xx}, \quad (22)$$

$$M_{yy} = a B (R_{yy} - R) + M, \quad (23)$$

$$M_{zz} = a B R_{zz}, \quad (24)$$

$$M_{xy} = \frac{R^{1/2}}{2q\Omega} [c_4 - (c_3 + c_5) B] M. \quad (25)$$

The remaining mixed components involving z vanish, i.e. $R_{xz} = R_{yz} = M_{xz} = M_{yz} = 0$. When $M = 0$, there is an explicit expression for R , derived by O03.

For the general case with $M \neq 0$, we did not find an analytic expressions for R and M in closed form. However, using the time-dependent equations it is possible to determine a linear fit of the form

$$R = R^{(0)} + \sum_{i=1}^5 r_i (c_i - c_i^{(0)}), \quad (26)$$

$$M = M^{(0)} + \sum_{i=1}^5 m_i (c_i - c_i^{(0)}), \quad (27)$$

where the $c_{1-5}^{(0)}$ are an approximation to the final fit parameters, and $R^{(0)}$ and $M^{(0)}$ are the corresponding numerically determined values of R and M . We are thus able to decrease the degree of freedom of the fitted system. We refine the parameters c_i with respect to the initial “guess” $c_i^{(0)}$ based on the quantity

$$\delta = [(M_{O03} - M_{\text{sim}})^2 + (R_{O03} - R_{\text{sim}})^2]^{1/2}. \quad (28)$$

In the analysis we seek the minimum value of δ .

4 Simulations

For the simulations we adopt a cubic computational domain of size $(2\pi)^3$. The gas is isothermal with constant sound speed c_s ; vertical gravity and stratification are omitted. The calculations are local and therefore made under the shearing box approximation (see below). The equations to be solved read

$$\frac{\mathcal{D}\rho}{\mathcal{D}t} = -\nabla \cdot (\rho \mathbf{u}), \quad (29)$$

$$\frac{\mathcal{D}\mathbf{u}}{\mathcal{D}t} = -(\mathbf{u} \cdot \nabla)\mathbf{u} - q\Omega_0 u_x \hat{\mathbf{e}}_y - 2\Omega_0 \hat{\mathbf{e}}_z \times \mathbf{u} - \frac{1}{\rho} \nabla p + \frac{1}{\rho} \mathbf{J} \times \mathbf{B} + \frac{1}{\rho} \nabla \cdot (2\nu \rho \mathbf{S}), \quad (30)$$

$$\frac{\mathcal{D}\mathbf{A}}{\mathcal{D}t} = \mathbf{u} \times \mathbf{B} + q\Omega_0 A_y \hat{\mathbf{e}}_x + \eta \nabla^2 \mathbf{A}, \quad (31)$$

where $\mathcal{D}/\mathcal{D}t = \partial/\partial t + U_0 \partial/\partial y$ includes the advection by the shear flow, \mathbf{u} is the departure from the mean flow \mathbf{U}_0 , ρ is the density, \mathbf{A} is the magnetic vector potential, $\mathbf{B} = \nabla \times \mathbf{A}$ is the magnetic field, and $\mathbf{J} = \nabla \times \mathbf{B}/\mu_0$ is the current density, μ_0 is the vacuum permeability, $S_{ij} = \frac{1}{2}(u_{i,j} + u_{j,i}) - \frac{1}{3}\delta_{ij} \nabla \cdot \mathbf{u}$ is the traceless rate of strain tensor, ν is the kinematic viscosity, and η is the magnetic diffusivity.

In order to get as close as possible to the ideal limit, we replace the diffusion terms by a hyperviscosity scheme, i.e. we replace the ∇^2 -operators by ∇^6 , aiming at maximizing the Reynolds number in the quiescent regions of the flow while diffusing and damping fluctuations near the grid scale. Compared to direct simulations (e.g. Haugen & Brandenburg 2006) with uniform viscosities, smaller grid resolution can be used to resolve the flow, which is crucial if the plan is to, e.g., undertake a parameter study, like in our case.

Periodic boundary conditions are applied in all three directions; in the radial direction we account for the shear flow \mathbf{U}_0 by making use of the shearing box approximation (e.g. Wisdom & Tremaine 1988):

$$f(\frac{1}{2}L_x, y, z) = f(-\frac{1}{2}L_x, y + q\Omega_0 L_x t, z), \quad (32)$$

where f stands for any of the seven independent variables, L_x stands for the radial extent of the computational domain, and t is the time.

The domain is initially threaded by a weak magnetic field,

$$\mathbf{A} = A_0 \hat{\mathbf{e}}_y \cos kx \cos ky \cos kz, \quad (33)$$

where $k = k_1$ has been chosen, and $k_1 = 2\pi/L_z$ is the smallest finite vertical wavenumber in the domain of height L_z . Thus, the magnetic field contains periodic x - and z -components with amplitude A_0 .

We choose the values of k_A , Ω_0 and A_0 so that the most unstable mode of the MRI, $k_{\max} = \Omega_0/u_A$ is well resolved by the grid; in practise this means that we always adopt $k/k_1 = 1$, $\Omega_0 = 0.2c_s k_1$ and $A_0 = 0.2\sqrt{\mu_0 \rho_0} c_s k_1^{-1}$, resulting in $k_{\max} = O(k_1)$. For the initial setup, the other condition for the onset of MRI, namely $\beta \gg 1$, where β is

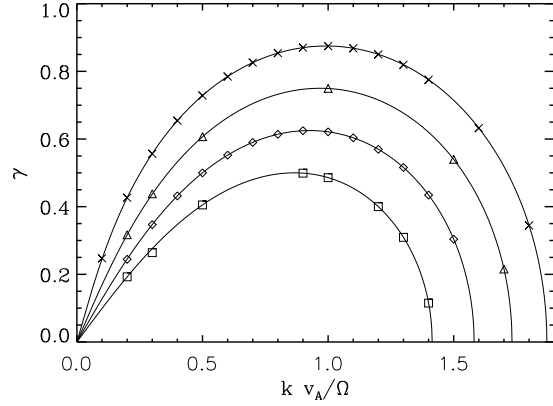


Fig. 1 Growth rates as a function of wavenumber from the 1D calculations. Crosses: $q = 1.75$, triangles: $q = 1.5$, diamonds: $q = 1.25$, squares $q = 1.0$. The solid lines represent the linear growth rates; see, e.g., PCP06.

the ratio of the thermal to magnetic pressure, is also satisfied as β is minimally 50 at the maximum values of the magnetic field. In all our runs the Mach number is well below unity, so compressibility effects are negligible.

For all the simulations we use the PENCIL-CODE¹, which is a high-order (sixth order in space, third order in time), finite-difference code for solving the MHD equations (Brandenburg & Dobler 2002).

The local calculations have been carried out at two different resolutions, namely 128 (in 1D) and 64^3 (in 3D); the corresponding numerical diffusion coefficients are $\nu_{\text{hyper}} = \eta_{\text{hyper}} = 3.5 \times 10^{-6}$ and 2.0×10^{-7} , respectively. The calculations were carried out on the IBM eServer Cluster 1600 at Scientific Computing Ltd., Espoo, Finland.

5 Results

5.1 Linear results

In order to make contact with the model of PCP06, we first aim at reproducing their theoretical linear results (see also Balbus & Hawley 1991) using one-dimensional calculations with an imposed magnetic field. We calculate several sets by fixing the shear rate ($q = 1.00, 1.25, 1.50, 1.75$) and angular velocity Ω_0 and varying the initial magnetic field strength B_0 . The growth rate and the stress ratio are monitored during the exponential growth of the instability. The results are displayed in Figs. 1 and 2.

As can be seen from Fig. 1, the linear growth rates can be reproduced by the numerical method quite accurately. From Fig. 2 it can be observed that the linear prediction (dotted curve) intercepts the numerical results (solid lines) exactly at k_{\max} for each q -curve. At each $k_{\max}(q)$, therefore, the linear prediction and numerical results show perfect agreement; see Eq. (4). In the 1D calculations, however,

¹ <http://www.nordita.org/software/pencil-code/>

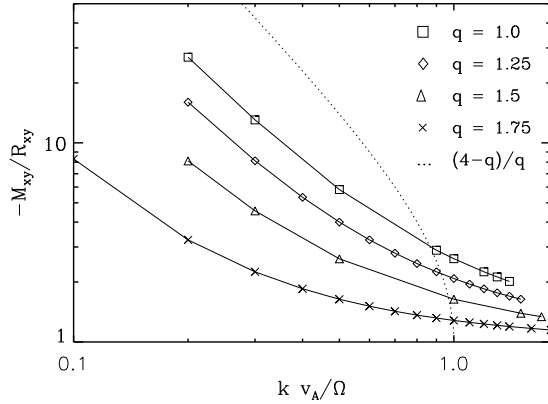


Fig. 2 Stress ratio $-M_{xy}/R_{xy}$ as function of wavenumber. The solid lines represent the linear 1D results with varying shear parameter q . The dotted line shows the linear prediction of PCP06 plotted for each $k_{\max}(q)$.

the system has not much freedom to create any other MRI mode than the one that is imprinted by the initial magnetic field strength, due to which the stress ratio is observed to vary as function of wavenumber, so that monotonically decreasing stress ratios are found with increasing wavenumber for all the q s investigated. This is clearly in disagreement with the PCP06 assumption, according to which the mode with k_{\max} should always get preferentially excited. The wavenumber dependence of the stress ratios, however, disappears in 3D: independent of the initial magnetic field strength, the mode with k_{\max} is observed to dominate. In that sense our 3D results are giving support to the basic assumption of PCP06, although, as will be discussed in the remaining part of the paper, the magnitudes and q -dependence of the stresses are otherwise different from the linear analysis.

5.2 Nonlinear results

We have performed a set of local calculations, in which we have fixed the angular velocity Ω_0 and the strength of the initial magnetic field, and then varied the shear parameter q . For the investigated range of shear parameters $0.4 \leq q \leq 1.9$, the maximally growing wavenumber, therefore, is varying according to Eq. (5), but is resolved by the numerical grid in all the calculations. We have checked that the resulting stresses are independent of the initial magnetic field strength (computations with initial plasma β of 20–800 were performed). This is particularly important in the net flux case (Blackman, Penna & Varniere 2008).

For smaller shear the stabilizing effect of vorticity is strong and the fluctuations grow larger than the stresses themselves; these calculations, therefore, are not included in the results. The data averaged over the nonlinear saturated stage (typically from a hundred to a few hundreds of

rotations) for the range $0.4 \leq q \leq 1.9$ is presented in Table 1.

As is evident from Table 1, both Reynolds and Maxwell stresses grow with the shear parameter q . The growth of the Reynolds stress is much stronger than the growth of the Maxwell stress, due to which the stress ratio (plotted in the second panel of Fig. 3) decreases as function of q . The simulated stress ratio significantly differs from the PCP06 linear prediction given by Eq. (6) and plotted in the figure with dotted lines. All the data points including the error bars are consistently larger than the prediction by a factor of 2–3.

Panel 1 of Fig. 3 shows the total stress, defined in Eq. (2), as a function of the shear-to-vorticity ratio, $q/(2-q)$. The shear-to-vorticity ratio is a quantity that is independent of the coordinate system, which was the main reason why Abramowicz et al. (1996) presented the stress as a function of this ratio. Interestingly, they found that the stress is a nearly linear function of the shear-to-vorticity ratio. This is confirmed by the new data. If one were to plot the stress as a function of q directly, the relation would become strongly nonlinear.

Also the magnetic to kinetic energy ratio (panel 6 in Fig. 3) exhibits q dependency, but it is less strong than that of the magnetic to kinetic stress ratio (panel 2 in Fig. 3). The energies are defined as $E_K = \frac{1}{2}\langle \rho u^2 \rangle$ and $E_M = \frac{1}{2}\langle B^2 \rangle$. Thus $E_K = \frac{1}{2}R$ and $E_M = \frac{1}{2}M$. Our results indicate that for flat (galactic) rotation curves with $q = 1$ the energy ratio should be a factor of two higher than for the case of Keplerian accretion disks ($q = 1.5$).

5.3 Predicting stresses with the O03 model

In their treatment, O03 use fiducial closure parameters $C_{1-5} = 1$ in order to demonstrate the overall behavior of the model. He recommends the parameters to be calibrated by comparison with numerical simulations in order to obtain more accurate predictions. We have made an attempt to determine the dimensionless closure parameters that work for each value of q in the range $0.4 \leq q \leq 1.9$.

There are essentially two ways to approach the problem. The first is to take the time independent equations (16)–(25) and solve for c_{1-5} using values of the traces R and M from the simulations. We call this method “backward modelling”. The problem with this method is that the Eqs. (16)–(25) are incomplete and do not set any constraints to the ratio M/R . Consequently, it does not produce the correct solution to the time dependent equations (7) and (8). Therefore we also used the linear approximation described by Eqs. (26) and (27) to improve the fit.

The second way of determining c_{1-5} is what we call “forward modelling”. The idea here is to seek such c_{1-5} that the results of the time-dependent equations (7) and (8) yield the same individual stresses and the traces R and M as the numerical simulations. This time a universal c_{1-5} is determined so that it predicts the stresses for all values $0.4 \leq q \leq 1.9$. Once a reasonably good set of c_{1-5} was

Table 1 Stress components averaged over the saturated regime of the local calculations. For the O03 closure model, $R_{xz} = R_{yz} = M_{xz} = M_{yz} = 0$.

| q | R_{xx} | R_{xy} | R_{yy} | R_{zz} | M_{xx} | $-M_{xy}$ | M_{yy} | M_{zz} | M/R |
|-----|---------------------|---------------------|---------------------|---------------------|---------------------|---------------------|---------------------|---------------------|-------|
| 0.4 | $5.3 \cdot 10^{-5}$ | $9.7 \cdot 10^{-6}$ | $2.1 \cdot 10^{-4}$ | $5.7 \cdot 10^{-5}$ | $1.3 \cdot 10^{-4}$ | $2.8 \cdot 10^{-4}$ | $1.2 \cdot 10^{-3}$ | $5.1 \cdot 10^{-5}$ | 4.4 |
| 0.5 | $7.8 \cdot 10^{-5}$ | $1.4 \cdot 10^{-5}$ | $3.8 \cdot 10^{-4}$ | $8.2 \cdot 10^{-5}$ | $1.5 \cdot 10^{-4}$ | $3.3 \cdot 10^{-4}$ | $1.5 \cdot 10^{-3}$ | $5.9 \cdot 10^{-5}$ | 3.1 |
| 0.6 | $1.2 \cdot 10^{-4}$ | $2.4 \cdot 10^{-5}$ | $4.1 \cdot 10^{-4}$ | $1.3 \cdot 10^{-4}$ | $2.1 \cdot 10^{-4}$ | $4.8 \cdot 10^{-4}$ | $2.1 \cdot 10^{-3}$ | $8.4 \cdot 10^{-5}$ | 3.6 |
| 0.7 | $1.9 \cdot 10^{-4}$ | $3.8 \cdot 10^{-5}$ | $9.0 \cdot 10^{-4}$ | $2.0 \cdot 10^{-4}$ | $2.7 \cdot 10^{-4}$ | $6.0 \cdot 10^{-4}$ | $2.5 \cdot 10^{-3}$ | $1.2 \cdot 10^{-4}$ | 2.2 |
| 0.8 | $2.0 \cdot 10^{-4}$ | $3.5 \cdot 10^{-5}$ | $8.9 \cdot 10^{-4}$ | $1.9 \cdot 10^{-4}$ | $2.1 \cdot 10^{-4}$ | $5.0 \cdot 10^{-4}$ | $2.3 \cdot 10^{-3}$ | $9.4 \cdot 10^{-5}$ | 2.0 |
| 0.9 | $3.2 \cdot 10^{-4}$ | $7.3 \cdot 10^{-5}$ | $7.0 \cdot 10^{-4}$ | $3.1 \cdot 10^{-4}$ | $3.7 \cdot 10^{-4}$ | $8.2 \cdot 10^{-4}$ | $3.4 \cdot 10^{-3}$ | $1.6 \cdot 10^{-4}$ | 2.0 |
| 1.0 | $4.2 \cdot 10^{-4}$ | $9.1 \cdot 10^{-5}$ | $6.3 \cdot 10^{-4}$ | $3.7 \cdot 10^{-4}$ | $3.8 \cdot 10^{-4}$ | $8.7 \cdot 10^{-4}$ | $3.6 \cdot 10^{-3}$ | $1.7 \cdot 10^{-4}$ | 2.9 |
| 1.1 | $6.6 \cdot 10^{-4}$ | $1.6 \cdot 10^{-4}$ | $8.5 \cdot 10^{-4}$ | $5.6 \cdot 10^{-4}$ | $6.0 \cdot 10^{-4}$ | $1.3 \cdot 10^{-3}$ | $4.8 \cdot 10^{-3}$ | $2.6 \cdot 10^{-4}$ | 2.7 |
| 1.2 | $8.6 \cdot 10^{-4}$ | $2.0 \cdot 10^{-4}$ | $1.1 \cdot 10^{-3}$ | $6.6 \cdot 10^{-4}$ | $6.4 \cdot 10^{-4}$ | $1.3 \cdot 10^{-3}$ | $5.0 \cdot 10^{-3}$ | $2.7 \cdot 10^{-4}$ | 2.3 |
| 1.3 | $1.7 \cdot 10^{-3}$ | $4.1 \cdot 10^{-4}$ | $1.8 \cdot 10^{-3}$ | $1.2 \cdot 10^{-3}$ | $1.3 \cdot 10^{-3}$ | $2.4 \cdot 10^{-3}$ | $8.4 \cdot 10^{-3}$ | $5.2 \cdot 10^{-4}$ | 2.2 |
| 1.4 | $2.5 \cdot 10^{-3}$ | $6.1 \cdot 10^{-4}$ | $2.2 \cdot 10^{-3}$ | $1.7 \cdot 10^{-3}$ | $1.8 \cdot 10^{-3}$ | $3.1 \cdot 10^{-3}$ | $1.1 \cdot 10^{-2}$ | $7.2 \cdot 10^{-4}$ | 2.1 |
| 1.5 | $2.7 \cdot 10^{-3}$ | $6.4 \cdot 10^{-4}$ | $2.0 \cdot 10^{-3}$ | $1.8 \cdot 10^{-3}$ | $1.6 \cdot 10^{-3}$ | $2.9 \cdot 10^{-3}$ | $9.8 \cdot 10^{-3}$ | $6.8 \cdot 10^{-4}$ | 1.9 |
| 1.6 | $3.7 \cdot 10^{-3}$ | $8.5 \cdot 10^{-4}$ | $2.3 \cdot 10^{-3}$ | $2.5 \cdot 10^{-3}$ | $1.8 \cdot 10^{-3}$ | $3.2 \cdot 10^{-3}$ | $1.0 \cdot 10^{-2}$ | $8.4 \cdot 10^{-4}$ | 1.6 |
| 1.7 | $6.3 \cdot 10^{-3}$ | $1.5 \cdot 10^{-3}$ | $3.7 \cdot 10^{-3}$ | $4.1 \cdot 10^{-3}$ | $2.9 \cdot 10^{-3}$ | $4.6 \cdot 10^{-3}$ | $1.5 \cdot 10^{-2}$ | $1.4 \cdot 10^{-3}$ | 1.3 |
| 1.8 | $8.9 \cdot 10^{-3}$ | $2.0 \cdot 10^{-3}$ | $4.4 \cdot 10^{-3}$ | $6.1 \cdot 10^{-3}$ | $3.4 \cdot 10^{-3}$ | $5.1 \cdot 10^{-3}$ | $1.6 \cdot 10^{-2}$ | $2.0 \cdot 10^{-3}$ | 1.1 |
| 1.9 | $1.8 \cdot 10^{-2}$ | $3.7 \cdot 10^{-3}$ | $6.2 \cdot 10^{-3}$ | $1.1 \cdot 10^{-2}$ | $4.8 \cdot 10^{-3}$ | $6.2 \cdot 10^{-3}$ | $1.8 \cdot 10^{-2}$ | $2.9 \cdot 10^{-3}$ | 0.7 |

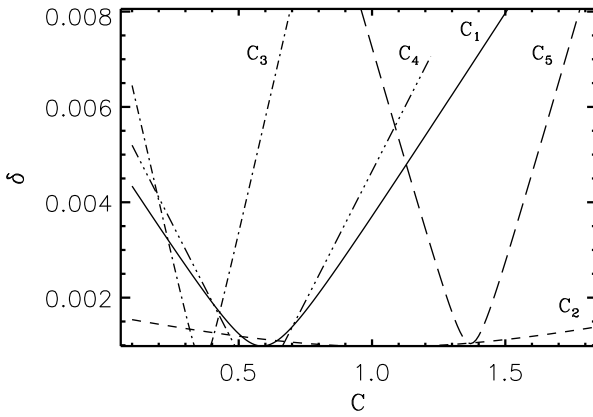


Fig. 4 The error estimate δ (see Eq. (28)) as a function of C .

found, the result was fine tuned further using the linear approximation given by Eqs. (26) and (27); see Figs. 4 and 5. From the Fig. 4 it can be seen that the best fit is obtained by fixing c_4 while keeping the other c_i unchanged.

The final closure parameters are thus $c_1 = 0.63$, $c_2 = 0.73$, $c_3 = 0.33$, $c_4 = 0.58$ and $c_5 = 1.35$, corresponding to $C_i = c_i L$ with $C_1 = 4.0$, $C_2 = 4.6$, $C_3 = 2.1$, $C_4 = 3.6$ and $C_5 = 8.5$. For these c_{1-5} the relevant fit parameters in Eqs. (26) and (27) are $R^{(0)} = 0.0057$ and $M^{(0)} = 0.013$ together with $r_1 = -0.0065$, $r_2 = -0.00012$, $r_3 = 0.024$, $r_4 = -0.010$, $r_5 = -0.0061$, and $m_1 = -0.0057$, $m_2 = -0.0012$, $m_3 = 0.0042$, $m_4 = 0.0038$, $m_5 = -0.018$.

6 Discussion

In this study we set out to investigate the shear rate dependency of MRI-generated turbulent stresses. We have performed a series of local shearing box simulations with vary-

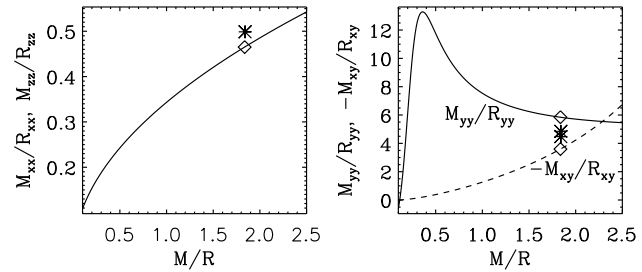


Fig. 5 Comparison of the simulation data (diamonds) to the chosen fit to Ogilvie model with $c_1 = 0.63$, $c_2 = 0.73$, $c_3 = 0.33$, $c_4 = 0.58$, $c_5 = 1.36$ (diamonds) for one particular run with $q=1.5$. The solid line shows the M/R -dependent result of the stationary equations with the chosen set of c -parameters. The additional constraint used in the fitting procedure required that the difference in the simulated and model M/R is minimal, due to which in this solution the values of M/R match while the individual stress ratios somewhat differ.

ing q and measured the resulting turbulent stresses. We find that the turbulent stress ratio $-M_{xy}/R_{xy}$, and the total stress T_{xy} exhibit strong q -dependency. The relation for the stress ratio by PCP06; see Eq. (6) predicts similar behaviour, but the ratio computed from the simulations is consistently 2-3 times larger than what their result indicates.

In order to further study the evolution of the MRI and the stresses we have attempted to reproduce them using the local closure model by O03. We first find a set c_{1-5} such that the time-dependent equations give the same individual stresses and traces R and M . The linear approximation of Eqs. (26)–(27) is then used together with the time-independent equations to improve the fit. The O03 closure parameters that describe our numerical simulation results

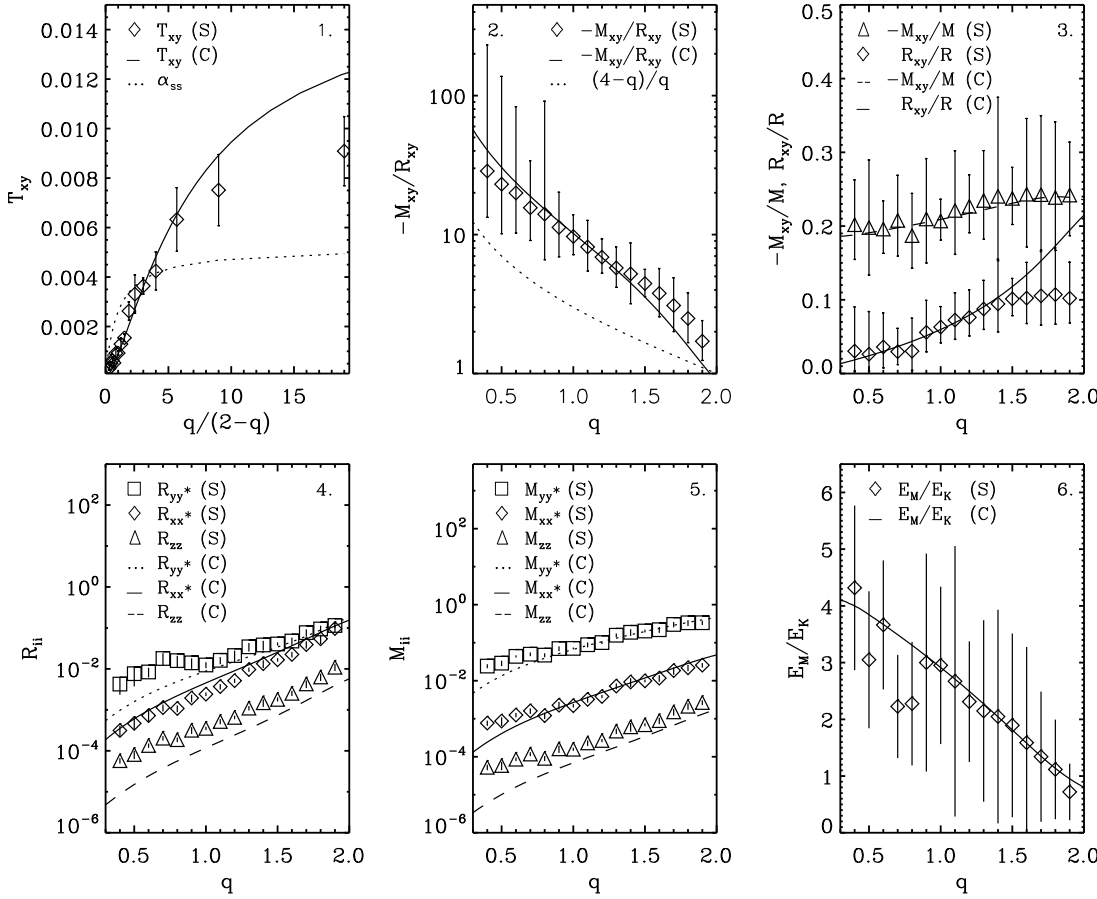


Fig. 3 Panel 1: total stress as a function of the shear-to-vorticity ratio, $q/(2-q)$, from the simulations (diamonds) and prediction from the O03 closure model (line) using $c_1 = 0.63$, $c_2 = 0.73$, $c_3 = 0.33$, $c_4 = 0.58$ and $c_5 = 1.35$. The error bars show the standard deviation of the quantity in question. Behaviour predicted by the Shakura-Sunyaev α viscosity model has been presented for comparison. Panel 2: stress ratio as a function of q from the simulations (diamonds), overplotted with the O03 closure result (solid line) and the PCP06 linear prediction (dotted line). Panels 3-5 show several stress component ratios from the simulations overplotted with the O03 closure results. To help visualisation, stress components R_{xx} , M_{xx} have been scaled up with a factor of 6, and R_{yy} , M_{yy} with a factor of 20. In panel 6, the ratio of magnetic to kinetic energy is presented. Throughout the figure, (s) is used to denote a simulation result and (c) a result given by the closure model.

are found to be $C_1 = 4.0$, $C_2 = 4.6$, $C_3 = 2.1$, $C_4 = 3.6$ and $C_5 = 8.5$.

The closure model by O03 was thus found to predict our simulation generated turbulent stresses quite well. The model certainly offers a much-needed method for studying the evolution of turbulent stresses in the shearing sheet limit. However, additional constraints for R and M are needed in order to determine the closure parameters C_i . The linear fitting approximation described in Eqs. (26) and (27) was devised to overcome this shortcoming.

Our results may also have some relevance in the galactic context, in which the MRI has been proposed to be responsible of the anomalous turbulent velocity dispersions found in the outer regions of some galaxies (e.g. Sellwood & Balbus 1999). On the other hand, the energy balance estimates from observations of NGC6949 (Beck 2004) indicate that magnetic energy could become dominant over the kinetic

energy in the outer regions of this galaxy, so that the energy ratio $E_M/E_K \approx 3-4$. According to our present results, in MRI-driven systems the magnetic energy clearly dominates over the kinetic energy for all $q < 1.6$, at the galactic value of $q = 1$ for flat rotation curves we find the value ≈ 3 , a number agreeing rather well with the observational estimates.

Acknowledgements. It is a pleasure to thank an anonymous referee for a comprehensive report that lead to significant improvements in the manuscript. The authors also wish to express their gratitude to Nordita for their hospitality during the program ‘Turbulence and Dynamos.’ We acknowledge the Scientific Computing Ltd., Espoo, Finland, for granting CPU time in their supercomputers. This work was supported by the Academy of Finland through grants No. 112020 (AJL) and No. 121431 (PJK) and in part by the National Science Foundation under grant PHY05-51164 (AB).

References

- Abramowicz, M., Brandenburg, A., Lasota, J.-P.: 1996, *MNRAS* 281, L21
- Armitage, P.J.: 1998, *ApJ* 501, 189
- Balbus, S.A., Hawley, J.F.: 1991, *ApJ* 376, 214
- Beck, R.: 2004, in *How does the galaxy work?*, ed. E.J. Alfaro, E. Pérez, & J. Franco, *ASSL* 315, 277
- Blackman, E.G., Penna, R.F., Varniere, P.: 2008, *New. A.* 13, 244
- Brandenburg, A., Nordlund, Å., Stein, R., Torkelsson U.: 1995, *ApJ* 446, 741
- Brandenburg, A., Dobler, W.: 2002, *Comp. Phys. Comm.* 147, 471
- Garaud, P., Ogilvie, G.I.: 2005, *J. Fluid Mech.* 530, 145
- Hawley, J.F., Gammie, C.F., Balbus, S.A.: 1995, *ApJ* 440, 742
- Hawley, J.F., Gammie, C.F., Balbus, S.A.: 1996, *ApJ* 464, 690
- Hawley, J.F., Balbus, S.A., Winters, W.F.: 1999, *ApJ* 518, 394
- Hawley, J.F.: 2001, *ApJ* 554, 534
- Haugen, N.E.L., Brandenburg, A.: 2006, *Phys. Fluids* 18, 075106
- Johansen, A., Klahr, H.: 2005, *ApJ* 634, 1353
- Kato S., Yoshizawa A.: 1995, *Publ. Astron. Soc. Jap.* 47, 629
- Käpylä, P.J., Brandenburg, A.: 2008, *A&A* 488, 9
- Lyra, W., Johansen, A., Klahr, H., Piskunov, N.: 2008, *A&A* 479, 883
- Ogilvie, G.I.: 2003, *MNRAS* 340, 969 (O03)
- Pessah, M.E., Chan, C.K., Psaltis, D.: 2006a, *MNRAS* 372, 183 (PCP06)
- Pessah, M.E., Chan, C.K., Psaltis, D.: 2006b, *PhRvL* 97, 1103
- Shakura N.I., Sunyaev R.A.: 1973, *A&A* 24, 337
- Sellwood, J.A., & Balbus, S.A. 1999, *ApJ* 511, 660
- Velikhov, E.P.: 1959, *Sov. Phys. JETP* 36, 1398
- Wisdom, J., Tremaine, S.: 1988, *AJ* 95, 925